Macedonian Veterinary Review Mac Vet Rev 2026; 49 (2): 181-194

Available online at
www.macvetrev.mk

Original Scientific Article

RADIOLOGICAL AND HISTOLOGICAL ASSESSMENT OF THE REGENERATION OF EXPERIMENTAL FRACTURES OF CRITICAL LENGTH, TREATED WITH HYDROXYAPATITE ALONE AND IN COMBINATION WITH AUTOLOGOUS PRP-GEL

Georgi Marinov Marinov[1], Nadya Zlatozareva Zlateva-Panayotova[1], Vesela Ivanova Todorova[2]

[1]Department of Surgery, Radiology, Obstetrics, and Gynecology, Faculty of Veterinary Medicine, University of Forestry, Sofia, Bulgaria
[2]Department of General and Clinical Pathology, Medical University-Sofia, Sofia, Bulgaria

Received 7 October 2025; Received in revised form 28 January 2026; Accepted 9 April 2026

ABSTRACT

The aim of this study was to evaluate the effect of autologous platelet-rich plasma (PRP) gel combined with nanohydroxyapatite (HA) on bone regeneration in critical-sized diaphyseal defects in rabbits. Fourteen clinically healthy adult New Zealand White rabbits were divided into two groups: control (HA only, n=7) and experimental (HA+PRP, n=7). Standardized defects were created in the radius (≥1.5× bone diameter), and radiological, histological, histochemical, and immunohistochemical analyses were performed on days 30, 60, and 90 post-surgery. Radiographically, the PRP group demonstrated earlier bone bridge formation and complete defect filling by day 90, with significantly higher healing coefficients (0.64 vs 0.21; $p<0.05$). Histological evaluation revealed accelerated callus maturation and active osteogenesis with organized bone marrow in the PRP group, whereas the HA group showed incomplete union and persistent fibrous tissue. Immunohistochemical staining (CD34) confirmed neovascularization and hematopoietic precursor cell proliferation in the PRP-treated defects. The combined use of nanohydroxyapatite and PRP gel significantly enhanced osteoregeneration and shortened healing time in critical-sized bone defects.

Key words: platelet-rich plasma, hydroxyapatite, bone regeneration, rabbit, histology

INTRODUCTION

Bones are among the most vulnerable part of the musculoskeletal system and are frequently subjected to severe trauma, accompanied by pain, impaired function and deformities. The bone tissue regeneration remains one of the major challenges in both human and veterinary orthopaedics due to the limited self-healing potential of extensive bone defects.

Corresponding author: Ch. Assist. Prof. Georgi Marinov Marinov, PhD
E-mail address: g.marinov@ltu.bg
Present address: Department of Surgery, Radiology, Obstetrics, and Gynecology, Faculty of Veterinary Medicine, University of Forestry, Sofia, Bulgaria
Phone: +359 889 502 915

Copyright: © 2026 Marinov G.M. This is an open-access article published under the terms of the Creative Commons Attribution License which permits unrestricted use, distribution, and reproduction in any medium, provided the original author and source are credited.

Competing Interests: The authors have declared that no competing interests exist.
Available Online First: 31 July 2026
Published on: 15 October 2026
https://doi.org/10.2478/macvetrev-2026-0021

Histologically, bone regeneration may occur via primary bone healing (direct contact <0.1 mm with lamellar bone formation), direct bone regeneration at larger interfragmentary distances (initial perpendicular orientation followed by remodeling), endochondral ossification (callus formation), or distant osteogenesis (callotasis) in large gaps (1). Fractures accompanied by critical-sized defects (CSD) rarely heal spontaneously and often result in delayed union, pseudoarthrosis, or complete non-union (2). This requires therapeutic support through autologous or allogeneic grafts and other strategies aimed at stimulating osteogenesis and restoring bone integrity. However, the limitations and morbidity associated with conventional reconstructive techniques have driven the search for alternative biologically based solutions. Surgical modulation of the local microenvironment using growth factors and pluripotent cells has therefore emerged as a modern, minimally invasive

approach with promising regenerative potential. Traditional treatment methods, such as osteosynthesis, autografts, allografts, and xenografts, have shown variable success and are frequently associated with complications including donor-site morbidity, graft rejection, infection, and poor integration (3, 4). As a result, an increasing attention has been directed toward regenerative medicine and bone tissue engineering approaches that aim to overcome these limitations by harnessing biological mechanisms of repair. These strategies combine biocompatible scaffolds, growth factors, and autologous cell derivatives to enhance osteogenesis (5, 6). Consequently, there is a clear clinical need for adjunctive, biologically active therapies that enhance bone regeneration while remaining safe, cost-effective, and suitable for routine veterinary conditions. Autologous platelet-rich plasma (PRP) and osteoconductive biomaterials, such as nanohydroxyapatite (HA), represent promising therapeutic optionsbecause they combine biological stimulation and structural support and can be readily integrated into standard surgical protocols without increasing immunological or infectious risks.

The ideal bone substitute should be biocompatible, bioresorbable, osteoconductive, and osteoinductive. No single material satisfies all requirements - nanohydroxyapatite provides excellent osteoconductivity, acting as a scaffold that facilitates regeneration and reconnection of bone fragments (7). PRP is a biocompatible and bioresorbable product, with minimal risk of immune reactions. Upon activation PRP releases multiple bioactive molecules that modulate cell migration, angiogenesis, and osteogenic differentiation, thereby exerting an osteoinductive effect within an appropriate microenvironment (8).

Literature data regarding the osteogenic potential of autologous PRP are mixed: some report a positive effect (8, 9), others have no effect or negative impact (10, 11). A key determinant of PRP efficacy is the method of application-activated versus non-activated PRP-as well as the preparation and storage protocol. Insufficient regenerative effects may result from inadequate biological activity or suboptimal release of growth factors, thereby limiting osteoblastic stimulation at the defect site. Activation with calcium-containing agents - calcium chloride (12), $CaCl_2$ + bovine thrombin (6), or calcium gluconate (13) - transforms PRP to a gel, enabling more sustained and concentrated release of growth factors and enhancing regenerative potential (3).

The present study aimed to address this research gap by evaluating the osteogenic potential of autologous calcium-gluconate–activated PRP gel combined with nanohydroxyapatite (experimental group-PRP) or nanohydroxyapatite alone (control group-HA) in a critical-sized rabbit radial defect model through radiological, histological, and immunohistochemical analyses.

It was hypothesized that the combination of nanohydroxyapatite and activated autologous PRP gel would result in faster and more complete bone regeneration compared to hydroxyapatite alone, through enhanced osteoinduction, angiogenesis, and early bone marrow formation.

MATERIAL AND METHODS

The studies were conducted in the period 2018-2021 at the University Clinic for Small Animals at the Faculty for Veterinary Medicine, University of Forestry, and the Faculty of Medicine, Medical University. All experiments were carried out in accordance with the European Convention for the Protection of Vertebrate Animals Used for Experimental and Other Scientific Purposes (ETS 123, Consil of Europe, 2007) and in accordance with Permit for the use of experimental animals No. 212/2018, entered in the register of the BFSA.

To minimize observer bias, radiological, histological, and immunohistochemical evaluations were performed in a blinded manner. The radiologists and histopathologist responsible for the assessments were not informed about the experimental grouping of the samples.

Experimental animals

The current study involved 14 rabbits aged between 12 and 18 months, divided equally by both sexes, weighing 3.2±0.6 kg. of the White New Zealand rabbit breed (*Oryctolagus cuniculus*). The sample size was determined based on previously published experimental studies using comparable CSD models in rabbits and similar outcome measures, rather than on a formal power analysis. The selected number of animals per group was considered sufficient to detect biologically relevant differences in radiological, histological, and immunohistochemical outcomes while complying with the principles of the 3Rs (Replacement, Reduction, and Refinement).

Prior to the start of the experiment, all animals underwent a one-month acclimatization period to the housing conditions and were fed a standard commercial rabbit diet supplemented with hay, according to the manufacturer's recommendations. All the rabbits were dewormed with fenbendazole (Panacur Paste, MSD) at a dose of 20 mg/kg for 7 consecutive days.

Groups

Following preliminary hematological (morphological and biochemical) and parasitological examinations, all animals were confirmed to be clinically healthy and were subsequently allocated into two experimental groups (n=7).

- Control group (HA) - the bone defect was filled only with nanohydroxyapatite (Hydroxyapatit nanopowder $HCa_5O_{13}P_3$, <200 nm particle size (BET), ≥97%, synthetic, Sigma-Aldrich® in combination with 0.2 mL vit. AD_3E.
- Experimental group (PRP) - the bone defect was filled with a combination of nanohydroxyapatite, 0.5 mL autologous PRP gel obtained after pre-activation with calcium gluconate (Calcium gluconicum 0.89%, Sopharma®) and 0.2 mL vit. AD_3E.

Obtaining PRP

Autologous blood (10 mL) was collected from the auricular vein of each rabbit into tubes containing 3.8% sodium citrate (blood-to-anticoagulant ratio 10:1) and maintained at 4 °C until processing. PRP was prepared immediately prior to surgery using a commercially available closed PRP preparation system (YCELL-BioPRPKit, YCELLBioMedical©), according to the manufacturer's general guidelines.

The PRP preparation protocol was based on the general principles described by Peng et al. (23) and subsequently optimized through preliminary testing to achieve reproducible and efficient platelet concentration using the available equipment. Immediately before the surgery, we transferred the blood to PRP separation tubes (YCELLBioMedical©, YCELL-BioPRPKit) and centrifuged it in a two-stage gradient tabletop centrifuge (Cence©, PRP500). The first centrifugation was done at 3,500 RPM (1,100 g) for 10 min for separation of the PRP and platelet-poor plasma (PPP) portions from the red blood cell fraction. The second centrifugation - at 2,500 RPM (600 g) for 3 min allowed the separation of PRP from PPP. After the second centrifugation we were able to aspirate approximately 0.5 mL of PRP.

PRP characterization

Although automated hematological analysis was initially attempted, platelet counts could not be reliably obtained using the Mindray BC-2800 analyzer, which repeatedly reported zero platelet values in PRP samples. This was most likely due to platelet aggregation following centrifugation and activation, a known limitation of impedance-based platelet counting systems when applied to concentrated platelet preparations.

Therefore, platelet concentration was assessed manually using light microscopy. Blood smears were prepared from both whole blood and PRP samples, stained using a Romanowsky-type staining (Diff-Quik staining protocol), and examined under a digital light microscope. Platelets were counted in multiple non-overlapping high-power fields with uniform cellular distribution, and the mean platelet count was calculated and converted to platelet concentration using a standardized multiplication factor.

Based on this approach, the platelet concentration in PRP samples was estimated to be approximately 2 times higher than baseline platelet levels measured in peripheral blood prior to PRP preparation. While this method does not provide precise absolute platelet counts, it enabled semi-quantitative comparison between whole blood and PRP confirming effective platelet enrichment.

Surgical protocol

Following anesthesia with xylazine hydrochloride (Xylazin 2%, Bioveta) at a dose of 5 mg/kg and ketamine hydrochloride (Anaket, Richter Pharma) at a dose of 50 mg/kg, administered muscularly and maintained with isoflurane (Isoflurin, Dechra) 3 vol.% a critical-sized defect was created in the radial diaphysis by performing two parallel transperiosteal osteotomies, resulting in a bone gap exceeding the transverse diameter of the radius (in our case within 7.3-7.6 mm). The defect was subsequently filled with the respective biomaterials according to the control and experimental group allocation, followed by routine soft tissue closure.

Radiological studies

Radiological examinations were performed immediately after the intervention (day 0), on the 30^{th}, 60^{th}, and 90^{th} day after the surgery in medio-lateral projection (Eckenmeyer Innovet X-ray).

The assessment of radiological signs was performed using a modified REBORNE scale (14), adapted by the authors to the specific characteristics of the experimental model and imaging protocol and based on predetermined radiographic signs of bone healing:

a. Enlargement of the defect and/or osteosclerosis of the edges - 0 pts.;

b. Lack of initiation for the formation of bone bridges - 1 pt.;
c. Beginning of the formation of bone bridges unilaterally - 2 pts.;
d. Beginning of the formation of bone bridges bilaterally - 3 pts.;
e. Formed bone bridges - 5 pts.;
f. Partial filling of the defect – 7 pts.;
g. Total filling of the defect with new bone tissue - 10 pts.;

Due to the limited number of animals at later time points, REBORNE scores are presented with measures of dispersion (mean ± SD and median with interquartile range) to better reflect score variability within each group.

At 30th, 60th, and 90th days two rabbits from each group were humanely euthanized under deep anesthesia with xylazine (5 mg/kg IM) and ketamine (50 mg/kg IM), followed by intravenous administration of propofol (10 mg/kg) and sodium pentobarbital (200 mg/kg). Death was confirmed by cessation of cardiac and respiratory activity. All procedures complied with Directive 2010/63/EU and the European Convention ETS 123, which define acceptable methods for humane euthanasia of laboratory animals.

Histological, histochemical, and immunohistochemical studies

Histological analysis

The obtained bone specimens were fixed in 10% neutral buffered formalin for 2-3 days, followed by decalcification in 10% EDTA solution for a period of three months. The samples were then embedded in paraffin blocks and sectioned at a thickness of 5 μm. The sections were washed, dehydrated in graded ethanol, and cleared in xylene. The resulting slides were stained with hematoxylin and eosin (H&E). Serial sections of 4-5 μm thickness were prepared using a rotary microtome (Leica RM2235, Germany).

For histological evaluation, the sections were stained with hematoxylin–eosin (H&E) to assess general morphology, cellular organization, and callus architecture. Microscopic observations were performed using a Leica DM2500 light microscope equipped with a Leica DFC295 digital camera.

Histochemical analysis

Bone samples were examined histochemically using the Masson-Goldner Trichrome Staining Kit (Merck, Germany). Connective tissue was selectively visualized through a combination of three different staining solutions: azofloxin and phosphotungstic acid (referred to as Orange G solutions) and triarylmethane (referred to as Light Green SF solution).

The Orange G solutions stain muscle tissue, cytoplasm, and erythrocytes, whereas the Light Green SF solution specifically stains connective tissue. Thus, cytoplasm and muscle fibers appear dark red, connective tissue and acidic substances are visualized in green, and erythrocytes appear orange.

Immunohistochemical analysis

Immunohistochemical examination was performed only on specimens with formed bone marrow within the callus. The tissue sections were deparaffinized and subjected to antigen retrieval in 1% trypsin solution (pH 1.8) for 60 min at 37.8 °C. The slides containing the histological fragments were then immersed in 3% hydrogen peroxide for 30 min to eliminate endogenous peroxidase activity, followed by incubation in 1% phosphate-buffered saline (PBS; pH 7.4).

The sections were incubated with the primary anti-OC antibody (Abcam, Cambridge, UK, dilution 1:200) and anti-PPAR-γ antibody (Santa Cruz Biotechnology, Dallas, TX, USA, dilution 1:150). The immunoreactive signal was visualized using a 3,3′-diaminobenzidine tetrahydrochloride (DAB) chromogen solution, producing a brown precipitate at the site of antigen localization.

Additionally, immunohistochemistry was performed with a monoclonal mouse anti-CD34 Class II antibody (Dako Agilent, USA) to evaluate angiogenesis and bone marrow neovascularization.

Statistical analysis

All results were presented as mean and mean±SD and were statistically processed using the ANOVA two-factor variance analysis, using the least-significant difference (LSD) post hoc test for the differences between the different groups compared to the control group. The non-parametric results were processed using the non-parametric Friedman test.

Differences with a significance level of $p<0.05$ were considered statistically significant.

RESULTS

Radiological studies

Control group (HA), ML-projection

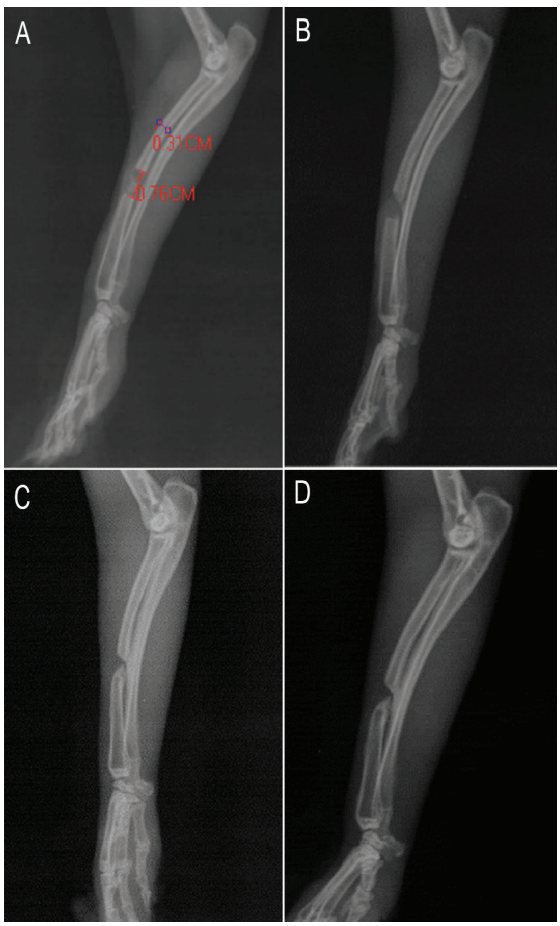


Figure 1. Radiological examinations of the radius in the control group (HA) in ML-projection - Day 0 (A), day 30 (B), day 60 (C), day 90 (D)

Radiological examination on day 0 in both groups show the size of the defect created, which is more than 2 times the diameter of the bone, and the lines of osteotomy are clearly visible. The inhomogeneous shadow at the site of the defect is due to the applied hydroxyapatite (Fig. 1A and 2A).

On the 30th day, in group HA, the lines of osteotomy have a smooth outline, rounded like a "fingertip", and in the ventrocaudal zone of the bony ends of the radius a slight promination is observed. In the area of the distal fragment, osteosclerosis is found, with the bone marrow canal partially closed, and a weak periosteal reaction on the dorsal side of the ulnar periosteum is also observed (Fig. 1B). On day 60, there is a decrease in the volume of the bone cavity, mostly in the palmar zone, as the bone marrow canal is closed and radiopacity of the accumulated callus is similar to that of the bone cortex. There are no formed bone bridges. Periosteal reaction is found only in the ventral zone of the fracture cavity (Fig. 1C).

Three months after osteotomy in the control group (HA), the volume of the fracture gap was reduced, with the newly formed bone tissue concentrated in the ventral area. The bone marrow canal is closed, and the density of the zone is equal to that of the cortex. The formed bone bridges are incomplete. An ulnar periosteal reaction is detected, ventral to the fracture cavity (Fig. 1D).

Experimental group (PRP), ML-projection

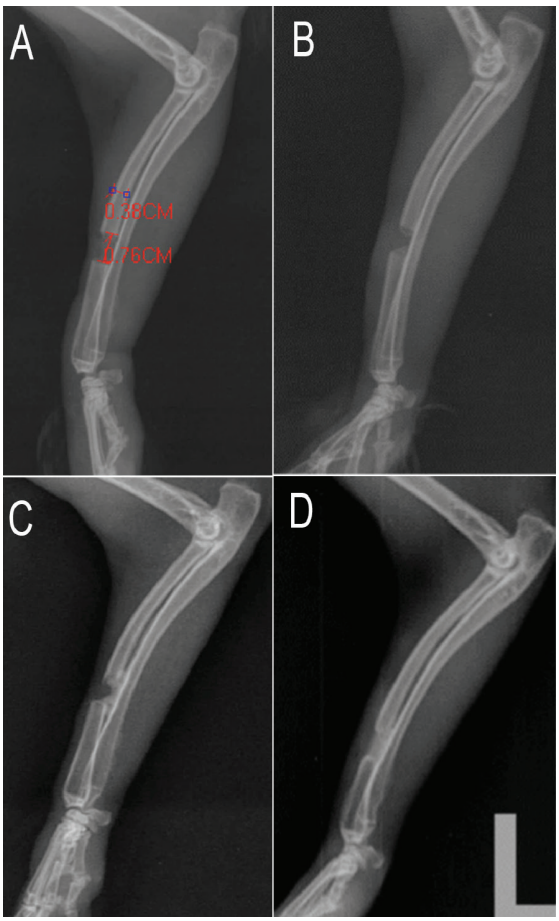


Figure 2. Radiological examinations of the radius in the experimental group (PRP) in ML-projection-Day 0 (A), Day 30 (B), day 60 (C), day 90 (D)

On the 30th day (Fig. 2B), the lines of osteotomy are visible, but in the area of the bone marrow canal, an inhomogeneous shadow with increased density is visible as a result of the accumulation of newly formed bone tissue. In the dorsal part of the defect

zone, moderate soft tissue edema is visualized.

On the 60th day (Fig. 2C), the newly formed bone tissue in the area of the defect occupies an area greater than 1/3 of the transverse diameter of the bone, and there is also a complete connection of the distal and proximal fragments through bone bridges.

Three months after the operation (Fig. 2D), the newly formed bone callus fills the bone defect, and the two fragments are united. The presence of hypercallus formation or periosteal reaction was not detected. The diameter of the bone callus at the proximal end is 20% smaller than that of the bone. A linear radiopaque shadow is established around the lines of osteotomy, the result of the initial accumulation of bone tissue and the closure of the bone marrow canal.

Summary data from radiological examinations

Based on the modified REBORNE score, the healing coefficient was significantly higher in the PRP-treated group compared to the HA control group at all evaluated time points (Table 1).

At day 30, the PRP group showed a significantly higher healing coefficient (median 0.21) compared to the control group (median 0.036; $p<0.01$).

At day 60, this difference became more pronounced, with the PRP group reaching a median healing coefficient of 0.64 versus 0.11 in the HA group ($p<0.05$).

Similarly, at 90 days, the PRP-treated defects maintained a significantly higher healing coefficient (median 0.64) compared to the control group (median 0.21; $p<0.05$), indicating sustained and superior radiological consolidation.

Histological and histochemical results

Control group (HA) at day 30

In the HA group, on the 30th day, the formation of cartilage callus is clearly visible (Fig. 3A). Fibrous connective tissue is also clearly differentiated (Fig. 3B), with chondrocytes and osteoblasts predominating in the callus zone (Fig. 3C). Masson histochemical examination (Fig. 3D) shows an initial process of osteogenesis.

Table 1. Radiological data evaluated according to seven characteristic signs of bone healing according to a modified REBORNE scale (14)

Day	group	Enlargement of the defect and/or osteosclerosis of the edges – 0 pts.	Lack of initiation for the formation of bone bridges – 1 pt.	Beginning of the formation of bone bridges unilaterally – 2 pts.	Beginning of the formation of bone bridges. bilaterally – 3 pts.	Formed bone bridges – 5 pts.	Partial filling of the defect – 7 pts.	Total filling of the defect with new bone tissue - 10 pts.	Group total, Median (IQR)	Healing coefficient (points/max)
30 (n=7)	HA		1						**1 (IQR 1–1)**	**0.036** (1/28)
	PRP		1	2	3				**6 (IQR 3–6)**	**0.21 **** (6/28)
60 (n=5)	HA		1	2					**3 (IQR 1-3)**	**0.11** (3/28)
	PRP		1	2	3	5	7		**18 (IQR 11–18)**	**0.64** (18/28)
90 (n=3)	HA		1	2	3				**6 (IQR 6-6)**	**0.21** (6/28)
	PRP		1	2	3	5	7		**18 (IQR 18–18)**	**0.64*** (18/28)

*p<0.05, **p<0.01, ***p<0.001 statistical reliability of the differences between the control and experimental groups in different periods. Scores are presented as median with interquartile range (IQR) to better reflect intra-group variability

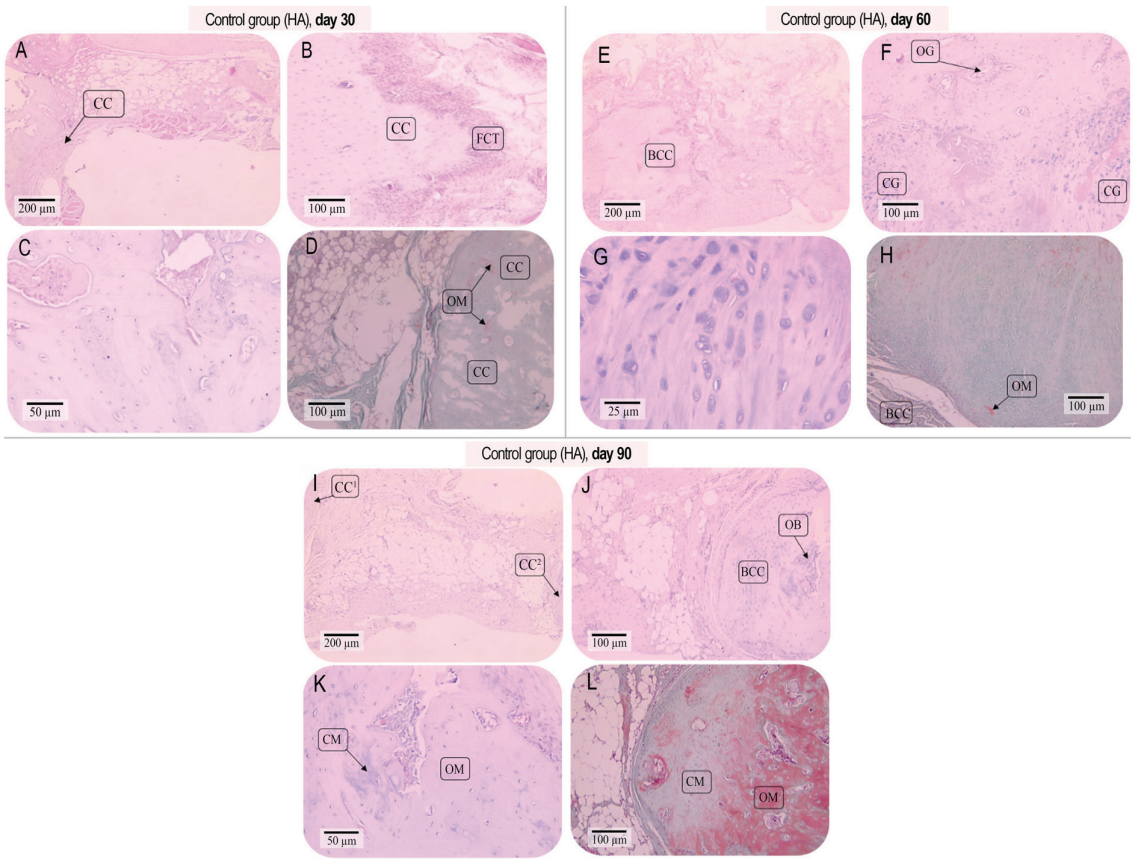


Figure 3. Histological results of the changes in the bone fragment in the control group (HA) at days 30, 60, and 90. Day 30-Cartilaginous callus (CC) and soft tissues (nervous, fat, and muscular) with a gap of ~4 mm (x5) (A), Cartilaginous callus (CC) and fibrous connective tissue (FCT) (x10) (B), Chondrocytes and osteoblasts (x20) (C), Histochemical results (Masson trichrome)-cartilaginous matrix (CC) and a minimal amount of osteoid (OM) matrix (x10) (D); Day 60-Formation of cartilage-bone callus (BCC) in contact with soft tissues (x5) (E), Active osteo-(OG) and chondrogenesis (CG) (x10, x40) (F), (G), Histochemical results (Masson trichrome) show deposition of osteoid matrix (OM) (x10) (H); Day 90-The proximal (CC^1) and distal (CC^2) cartilaginous callus are separated by soft tissues (±2 mm) (x5) (I), Active osteoblastic activity (OB) observed with separate cartilaginous foci with active osteogenesis (x10), (J), Cartilage (CM) and osteoid (OM) matrix are presented (x20) (K), Histochemical results (Masson trichrome)-distribution of cartilage (CM) and osteoid matrix (OM) around the cartilage-bone callus, in contact with soft tissues (x10) (L)

Lack of healing and contact between cartilage-bone callus and soft tissues is detected on the 60th day (Fig. 3F). Chondro- and osteogenesis is active, but bone callus is absent (Fig. 3G). Histochemically, focal production of osteoid matrix is detected (Fig. 3H).

On the 90th day, persistent non-union of bone fragments was observed in group HA (Fig. 3I), but active osteoblastic activity was detected close to the bone-cartilage callus (Fig. 3J, BCC). Cartilage and osteoid matrix were detected (Fig. 3K).

On histochemical examination (Fig. 3L), approximately equal amounts of cartilaginous and osteoid matrix were observed.

Experimental group (PRP)

In the PRP experimental group, as early as the 30th day, a bone callus (OC) was detected, connecting the ends of the two bone fragments (Fig. 4A). In the area of the forming bone callus, active osteogenesis is clearly observed (Fig. 4B). The Masson histochemical examination (Figs. 4C, D) showed a dominant amount of bone matrix and minimum amount of cartilaginous matrix, which is indicative of an accelerated process of maturation of the bone callus.

Two months later, a bone callus with tunneling bone marrow was histologically detected, which

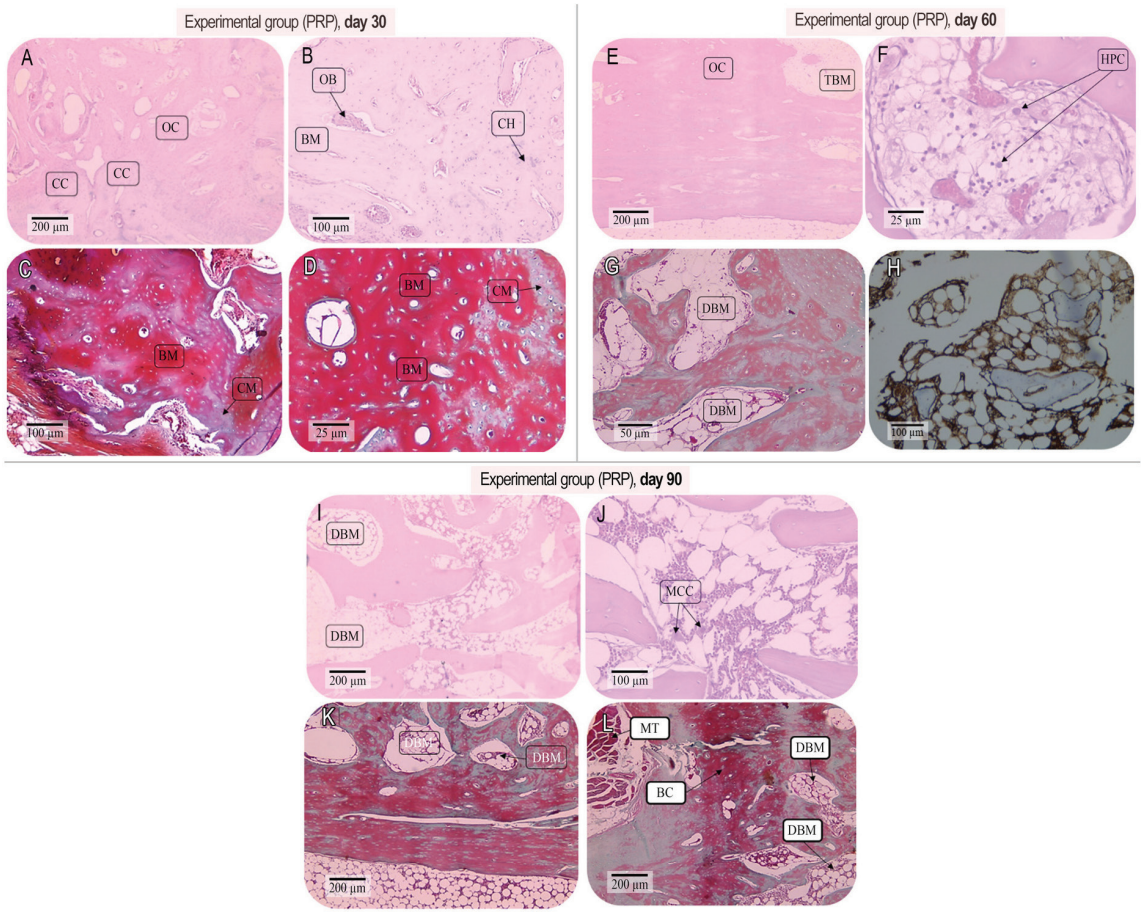


Figure 4. Histological results of the changes in the bone fragment in the experimental group (PRP) at days 30, 60, and 90. Day 30-Bone callus formation (OC). In the lower part of the histosection, a prominent cartilaginous "cap" of the callus (CC) is found, which originates from the ulna (x5) (A), Zone of active osteogenesis – formed bone matrix (BM) with groups of osteoblasts (OB) and small groups of chondrocytes (CH) (x10) (B), Histochemical results (Masson trichrome) - bone matrix (BM, red) and cartilaginous matrix (CM, green) (x10), (x40) (C), (D); Day 60-Bone callus (OC) with tunneling bone marrow (TBM) (x5) (E), Presence of hematopoietic precursor cells (HPC) (x40) (F), Histochemical results (Masson trichrome)-presence of differentiated bone marrow (DBM) is observed (x20) (G), Immunohistochemistry - hematopoietic precursor cells and angioblastic composition, CD34, Dako Agilent, (x10) (H); Day 90-Bone marrow (DBM) spaces of different sizes (x5) (I), Megakaryocytes (MCC), showing abnormal topographic distribution within the bone marrow, characterized by clustering and displacement toward trabecular surfaces (x40) (J), Histochemical results (Masson trichrome)-bone callus with formed bone marrow (DBM) in contact with the bone marrow and the ulna compact (below) (x20) (K), Muscle tissue (MT) between the two bones, interrupted by bone callus (BC) with formed bone marrow (DBM) (x20) (L)

came into contact with the compact and bone marrow of the adjacent bone (ulna, below) (Fig. 4E). Hematopoietic precursor cells without morphologically recognizable signs of maturation in the newly formed bone marrow was also detected (Fig. 4F). Histochemically, a differentiated bone marrow is observed (Fig. 4G), indicating the formation of spongy bone in the pathological area. Immunohistochemistry shows indication of hematopoiesis, with an increased number of hematopoietic precursor cells (Fig. 4H).

At the 3rd month, bone marrow spaces of different sizes are found in the bone callus (Fig. 4I) exhibiting active hematopoiesis with a predominance of erythroblastic lineage and the presence of megakaryocytes. These megakaryocytes preserved typical cell size, multilobulated nuclei, and characteristic cytoplasmic features, consistent with morphologically mature megakaryocytes, indicating functional reconstitution of the bone marrow microenvironment within the regenerated tissue (Fig. 4J). Histochemical examination on

day 90 demonstrated complete bridging of the defect by a mature bone callus connecting the two fracture ends (Fig. 4K). Muscle tissue was observed adjacent to the regenerated area, interrupted by newly formed bone callus, containing organized bone marrow spaces, indicating advanced tissue remodeling (Fig. 4L).

DISCUSSION

Critical-sized defects (CSD) are defined as the smallest wound that does not heal spontaneously over a long period of time (15, 16). While this concept is well established, the exact dimensional definition of the defect may vary depending on animal age, bone type, biomechanical loading, and periosteal preservation. Previous studies using rabbit radial defect models have reported variability in the minimal defect length required to prevent spontaneous healing, with suggested thresholds ranging from approximately 10 mm to more than 14 mm. In particular, a recent study conducted in 6-month-old New Zealand white rabbits proposed that defects greater than 1.4 cm are required to consistently meet the criteria of a CSD (17). However, older animals demonstrate reduced regenerative capacity compared to younger individuals, which may lower the threshold at which spontaneous healing becomes unlikely. In the present study, the observed healing pattern corresponded to distant osteogenesis with initial fibrous callus formation rather than direct bone regeneration, supporting the classification of the defect as functionally critical within the context of this experimental model. Therefore, the selected defect size was considered appropriate to evaluate the osteogenic potential of the applied biomaterials.

Predicting progression toward union or non-union is crucial for timely decisions. A suggestive radiological indicator of non-union is rounding of the fragment ends ("finger-like"), with increased radiodensity in the gap due to hypertrophic shaft and medullary canal closure, which may obstruct bridge formation (18). Hallmark signs of early healing are periosteal callus accumulation, bony bridges, and filling of the gap with blurring or disappearance of the fracture line. Salih et al. (19) describe the "^" sign in the gap with predictive value for union versus non-union; in the presence of osteosynthetic material, longer retention is recommended. Based on literature and clinical experience, we monitored healing using imaging at defined periods, focusing on the adapted REBORNE criteria. The limited number of animals, particularly at the 60- and 90-day time points, should be considered when interpreting the results. For this reason, radiological scores were analyzed with additional dispersion measures (mean±SD and median with interquartile range) to better illustrate intra-group variability, similar to the method, used by Gómez-Barrena et al. (20). Nevertheless, the consistent progression of radiographic features across time points supports the robustness of the observed healing patterns.

One month postoperatively, in the hydroxyapatite (HA) control group-where only an osteoconductive material was applied-the osteotomy lines appeared rounded without radiographic signs of bridge initiation. By day 60, a hypertrophic shaft and medullary canal occlusion by tissue with cortical-like radiodensity were present. These features indicate healing without bridging in the control (HA) group. In contrast, the PRP-treated group demonstrated earlier and more organized reparative activity. PRP application resulted in progressive bone bridge formation by day 60 and complete defect filling by day 90, without hypercallus formation or excessive periosteal reaction. These findings indicate that PRP accelerated the transition from early reparative changes to stable structural union compared to the osteoconductive scaffold alone (10).

The histological progression observed in both groups revealed distinct regenerative pathways that align with previously described mechanisms of bone healing (1). In the HA group by day 30, the presence of a cartilaginous callus and centrally located fibrous tissue indicated that healing had entered the early chondrogenic phase, yet without sufficient osteogenic progression. Similar findings have been reported in defect models where osteoconductive scaffolds were applied without osteoinductive stimulation (4, 10). By the 60th day, histological examination showed a cartilage–bone callus in contact with soft tissue but lacking complete union between the bone ends. The formation of focal osteoid islands and active chondro- and osteogenesis suggested that local repair activity was ongoing but spatially restricted, likely due to the absence of strong angiogenic and cellular signals. These findings are consistent with earlier studies where hydroxyapatite served mainly as a passive scaffold for bone ingrowth, exhibiting delayed mineralization and reduced marrow organization (1, 7). At 90 days, persistent non-union with active osteoblastic foci and parallel zones of cartilage and osteoid tissue confirmed that the repair process in the HA group followed

a delayed distant osteogenesis (callotasis) pattern, characterized by gradual endosteal proliferation without central bridging. This outcome parallels reports by Özak et al. (11), who demonstrated that scaffold-only approaches often lead to incomplete regeneration, with fibrous encapsulation at the defect margins and limited vascular penetration.

In contrast, the PRP-treated group demonstrated a markedly different histological profile consistent with accelerated and organized bone regeneration. By day 30, a well-defined bone callus bridged the defect, with a predominance of osteoblasts and newly formed bone matrix. The presence of a cartilaginous "cap" overlying the callus suggested the coexistence of endochondral ossification, a physiological mechanism that provides structural stability during early bone repair. These early histological features correspond to the initial osteogenic phase described in PRP-augmented models, where platelet-derived growth factors promote osteoblast differentiation and matrix mineralization (5, 8). Histochemical staining with Masson–Goldner trichrome at this stage revealed a dominant bone matrix with minimal cartilage, confirming that the mineralization process was initiated earlier compared to the control group. The red-stained areas of bone matrix and the scarce green cartilaginous components indicated an advanced maturation of the callus, consistent with reports that PRP accelerates the transition from chondrogenic to osteogenic tissue (9). At 60 days, histological examination demonstrated well-formed bone callus containing tunneling bone marrow, indicating both structural and functional regeneration. The detection of hematopoietic precursor cells (HPCs) and early bone marrow differentiation suggests that PRP not only accelerated osteogenesis but also promoted angiogenesis and hematopoietic niche reestablishment. The presence of CD34-positive endothelial progenitors, identified immunohistochemically, further supports the activation of neovascularization within the regenerating area. These results align with the findings of Yin et al. (8), who documented that PRP enhances bone healing through synergistic osteogenic–angiogenic effects mediated by VEGF and PDGF signaling pathways. By day 90, the PRP group exhibited complete bridging of the defect by a mature bone callus with organized bone marrow spaces and active hematopoiesis, as well as the presence of morphologically mature megakaryocytes within newly formed bone marrow spaces, indicating reestablishment of bone marrow architecture and hematopoietic activity. The presence of mature megakaryocytes indicates functional reconstitution of the bone marrow during advanced bone regeneration.

The intimate contact between the new callus and the adjacent ulnar compact bone confirmed the integration of the regenerated tissue into the pre-existing cortical structure. The histochemical findings, showing the coexistence of bone marrow, muscle tissue, and mineralized trabeculae, demonstrate that PRP not only accelerated osteogenesis but also guided the remodeling process toward lamellar bone formation, consistent with physiological healing patterns (1). The immunohistochemical results provide additional evidence of PRP-induced angiogenesis and marrow reconstitution. The presence of CD34-positive endothelial and angioblastic cells at day 60 correlates with the observed vascularization of the callus, which is essential for nutrient delivery and bone tissue maturation (21). These findings are in agreement with Abdel-Haffiez and Khalil (9), who reported increased angiogenic and osteogenic marker expression following PRP administration in rabbit models, and with Singh et al. (3), who emphasized the interdependence of vascular and osteogenic pathways during early bone regeneration.

Among the variables affecting PRP efficacy is platelet activation, which alters both the quantity and kinetics of released molecules. There is no consensus on the optimal activation method; choice is often pragmatic. The blood clot is critical: if fibrin degradation is not synchronized with bone regeneration, healing may be impaired. The use of calcium gluconate as an activator converted PRP into a stable fibrin gel that acted as both a mechanical matrix and a biochemical reservoir. This dual function is essential for bone healing. The fibrin structure not only maintains the growth factors at the defect site but also allows their sustained and gradual release, mirroring natural wound-healing dynamics (21, 22).

Consistent with these histological and immunohistochemical data, the healing pattern identified in our model - characterized by early vascularized callus and the coexistence of cartilaginous and osteoid matrices - corresponds to a mixed form of bone regeneration involving both distant osteogenesis and endochondral ossification. This hybrid mechanism is typical for large bone gaps, where direct bone contact between fragments is not achievable (1), and cartilage intermediate formation precedes mineralization and remodeling (2). The presence of hypertrophic chondrocytes and the progressive replacement of cartilaginous matrix

by osteoid tissue observed histologically are classic features of endochondral remodeling, confirming that the regenerative process proceeded through physiological pathways. The early appearance of bone marrow spaces and hematopoietic precursor cells in the PRP group further supports that PRP accelerates marrow organization, likely through enhanced angiogenesis and mesenchymal recruitment, as previously described by Singh et al. (3) and Yin et al. (8). The involvement of the ulnar periosteum likely contributed to the rapid bridging, as periosteal osteoprogenitors are known to enhance callus formation in forearm defect models (18). Peng et al. (23), on the other hand, reported that the addition of PRP to bovine-derived xenografts in peri-implant defects of the rabbit tibia did not enhance bone formation and may even delay peri-implant healing. These results differ from the present study, where PRP combined with nanohydroxyapatite resulted in accelerated callus formation, earlier endochondral bridging, and advanced marrow reconstitution. These differences, compared to our study, may be explained by fundamental differences in the biological and mechanical environment of the defect models as well as in the scaffold properties. In the study by Peng et al. (23), PRP was applied around titanium implants in a peri-implant setting, where bone regeneration is strongly influenced by implant surface characteristics, and stress shielding. Moreover, bovine-derived xenografts primarily act as passive space fillers with limited resorption dynamics, whereas nanohydroxyapatite provides a bioactive osteoconductive scaffold that more closely mimics native bone mineral and supports vascular and cellular invasion.

Our findings are in accordance with several previous investigations that demonstrated enhanced bone regeneration when PRP was used in conjunction with osteoconductive scaffolds such as HA or β-tricalcium phosphate (7, 23). However, results across studies remain heterogeneous. Some authors have reported limited or absent regenerative benefit of PRP when used alone or without proper activation (10, 11). The main sources of inconsistency include variations in platelet concentration, presence of leukocytes, centrifugation protocols, and activation methods (6). The current findings reinforce the idea that PRP functions primarily as a biological enhancer, whose success depends on the surrounding matrix and the method of activation. When combined with nanohydroxyapatite, which serves as a structurally stable and biocompatible scaffold, PRP augments cellular migration and vascular invasion—two processes critical for converting the initial fibrous callus into organized bone tissue (2).

According to our findings, adding activated autologous PRP gel to an osteoconductive HA scaffold shifts healing of a critical-sized radial defect from a predominantly distant osteogenesis pattern toward a mixed pathway that includes earlier endochondral bridging, marrow tunneling, and vascular/marrow maturation by 60-90 days.

The enhanced osteogenic response observed in the PRP-treated group is likely related to two synergistic mechanisms: (1) early activation of osteoinductive and angiogenic signaling, and (2) the creation of a stable fibrin-based microenvironment that sustains local growth factor release. Activated PRP is known to deliver concentrated levels of PDGF, TGF-β, VEGF, IGF, EGF, and FGF, all of which stimulate osteoblast differentiation, mesenchymal stem cell recruitment, and neovascularization (5, 8). The early appearance of marrow spaces and CD34-positive endothelial precursors in our study is consistent with the pro-angiogenic role of PRP, which has been recognized as a prerequisite for successful osteogenesis (3, 9).

Our findings in this study are partly consistent with, but also extend, the observations reported in the calvarial defect model using PRP combined with a β-tricalcium phosphate scaffold (24). In both studies, PRP did not act as an independent osteogenic substitute but functioned as a biological enhancer whose efficacy depended on the presence of an osteoconductive matrix. Similar to their observations, PRP application in our study was associated with an early inflammatory and angiogenic response, followed by enhanced recruitment of osteoprogenitor and endothelial cells, supporting the concept that PRP primarily modulates the biological microenvironment rather than directly inducing mineralization. However, important differences between the models should be emphasized. The calvarial model involved a non–load-bearing flat bone with periosteal removal and demonstrated delayed but sustained osteogenesis without complete defect closure. In contrast, our radial defect model represents a long-bone environment with partial mechanical stability provided by the intact ulna and preserved periosteal contribution. Under these conditions, PRP combined with nanohydroxyapatite promoted earlier endochondral bridging, accelerated marrow tunneling, and functional bone marrow reconstitution by 60-90 days, resulting in complete defect bridging.

Studies evaluating PRP in combination with biomaterial scaffolds for osteochondral repair, including composite systems based on hydroxyapatite and polymeric matrices, have shown that PRP application primarily promotes tissue neoformation, enhances vascularization, and improves bone–implant interface maturation, while differences between treatment groups were often quantitative rather than qualitative (25). Similarly, our results confirm that PRP acts as a biological enhancer rather than an independent osteogenic substitute, amplifying the regenerative response initiated by an osteoconductive matrix that permit vascular invasion and marrow organization.

These differences highlight that PRP-driven regeneration is highly context-dependent and influenced by bone type, mechanical environment, and periosteal integrity.

While these results are encouraging, they must be interpreted within the limitations of the experimental model. The rabbit radius, supported by an intact ulna, provides partial mechanical stability, potentially facilitating union compared to load-bearing long bones (26). Nevertheless, the model remains well-established for assessing osteoconductive and osteoinductive properties of biomaterials. Another factor to consider is that PRP composition was not quantified in terms of platelet count or cytokine content, which may vary between individuals and influence biological potency (5). Despite these potential sources of variability, the consistency of radiological, histological, and immunohistochemical findings across multiple time points strengthens the reliability of the observed effect.

Future research should focus on refining and expanding the translational potential of PRP-based bone regeneration strategies. Specifically, future studies should aim to quantify and standardize PRP composition, including platelet and leukocyte ratios as well as growth factor concentrations, to ensure reproducibility and comparability across experiments (27). Comparative analyses of different activation agents such as calcium chloride, calcium gluconate, and thrombin, along with various delivery formats (liquid, gel, or scaffold-impregnated), would clarify their relative efficacy and release kinetics. In addition, combining radiological, biomechanical, and molecular endpoints—including markers such as RUNX2, COL2A1, and VEGF—would provide a more comprehensive evaluation of osteochondral repair dynamics. Finally, validation of the present findings in load-bearing defect models and in clinical veterinary applications, as well as assessment of potential synergistic effects with bone marrow aspirate concentrate or mesenchymal stem cells, could further establish the therapeutic value and clinical applicability of PRP-enhanced bone regeneration (5, 8).

In summary, the findings of this study indicate that the integration of an osteoconductive scaffold (HA) with a biologically active matrix (PRP) creates a microenvironment that enhances osteogenesis through stimulation of angiogenesis, acceleration of osteoid formation, and early bone marrow development. Moreover, the use of calcium gluconate activation, rather than thrombin, could simplify intraoperative procedures while maintaining the desired biological efficacy (13, 27). The current evidence supports the hypothesis that activated autologous PRP gel enhances the regenerative potential of hydroxyapatite in critical-sized bone defects. This combination therefore represents a promising strategy for advancing regenerative orthopedics in both experimental and clinical settings (5, 8, 9).

CONCLUSION

Nanohydroxyapatite is a highly suitable synthetic bone substitute that can be effectively used as an osteoconductive material. The application of platelet-rich plasma (PRP) gel represents a promising approach that activates, stimulates, and accelerates osteoregenerative processes in critical-sized bone defects. The activation and conversion of PRP into a gel prior to application is an essential step, as it enhances integration with the osteoconductive scaffold, ensures stable retention at the defect site, and allows for the gradual release of growth factors. The comprehensive histological, histochemical, and immunohistochemical analyses performed in this study at different stages of bone healing are in full agreement with the radiological findings, collectively confirming the strong osteogenic potential of topically applied PRP gel.

CONFLICT OF INTEREST

The authors declare that they have no financial or non-financial conflict of interest regarding authorship and publication of this article.

ACKNOWLEDGMENTS

The research was supported by the University of Forestry and Medical University of Sofia.

AUTHORS' CONTRIBUTION

GM conceived and designed the experimental study, participated in the the surgical procedures and in vivo experiments, coordinated data collection, and was the primary contributor to data analysis and manuscript drafting. NZZP contributed to the experimental design, preparation and standardisation of biomaterials (platelet-rich plasma and hydroxyapatite), participated in the surgical interventions, and critically reviewed the manuscript. VIT was responsible for histological processing, histochemical and immunohistochemical evaluation, interpretation of microscopic findings, and contributed to the analysis of histological results.

REFERENCES

1. Li, X., Xu, H., Zhao, B., Jiang, S. (2018). Accelerated and enhanced osteointegration of MAO-treated implants: histological and histomorphometric evaluation in a rabbit model. Int J Oral Sci. 10, 11. https://doi.org/10.1038/s41368-018-0008-z PMid:29563493 PMCid:PMC5944253

2. Alonso-Fernández, I., Haugen, H.J., Nogueira, L.P., López-Álvarez, M., González, P., López-Peña, M., et al. (2024). Enhanced bone healing in critical-sized rabbit femoral defects: impact of helical and alternate scaffold architectures. Polymers (Basel). 16(9): 1243. https://doi.org/10.3390/polym16091243 PMid:38732711 PMCid:PMC11085737

3. Singh, R., Rohilla, R., Gawande, J., Sehgal, P. (2017). To evaluate the role of platelet-rich plasma in healing of acute diaphyseal fractures of the femur. Chin J Traumatol. 20(1): 39-44. https://doi.org/10.1016/j.cjtee.2016.03.007 PMid:28202370 PMCid:PMC5343097

4. Mooren, R.E., Merkx, M.A., Bronkhorst, E.M., Jansen, J.A., Stoelinga, P.J. (2007). The effect of platelet-rich plasma on early and late bone healing: an experimental study in goats. Int J Oral Maxillofac Surg. 36(7): 626-631. https://doi.org/10.1016/j.ijom.2007.03.013 PMid:17521885

5. Oryan, A., Alidadi, S., Moshiri, A. (2015). Platelet-rich plasma for bone healing and regeneration. Expert Opin Biol Ther. 16(2): 213-232. https://doi.org/10.1517/14712598.2016.1118458 PMid:26561282

6. Sadeghi-Ataabadi, M., Mostafavi-Pour, Z., Vojdani, Z., Sani, M., Latifi, M., Talaei-Khozani, T. (2017). Fabrication and characterization of platelet-rich plasma scaffolds for tissue engineering applications. Mater Sci Eng C Mater Biol Appl. 71, 372-380. https://doi.org/10.1016/j.msec.2016.10.001 PMid:27987720

7. Molina-Miñano, F., López-Jornet, P., Camacho-Alonso, F., Vicente-Ortega, V. (2009). Plasma rich in growth factors and bone formation: a radiological and histomorphometric study in New Zealand rabbits. Braz Oral Res. 23(3): 275-280. https://doi.org/10.1590/S1806-83242009000300009 PMid:19893962

8. Yin, N., Wang, Y., Ding, L., Juan, J., Du, L., Zhu, Z., Pan, M., et al. (2020). Platelet-rich plasma enhances the repair capacity of muscle-derived mesenchymal stem cells to large humeral bone defect in rabbits. Sci Rep. 10, 6771. https://doi.org/10.1038/s41598-020-63496-5 PMid:32317711 PMCid:PMC7174361

9. Abdel-Haffiez, S.H., Khalil, N.M. (2024). Effect of platelet rich plasma injection on bone formation in the expanded mid-palatal suture in rabbits: a randomized controlled animal study. BMC Oral Health. 24(1): 167. https://doi.org/10.1186/s12903-024-03922-6 PMid:38308245 PMCid:PMC10835953

10. Galanis, V., Fiska, A., Kapetanakis, S., Kazakos, K., Demetriou, T. (2017). Effect of platelet-rich plasma combined with demineralised bone matrix on bone healing in rabbit ulnar defects. Singapore Med J. 58(9): 551-556. https://doi.org/10.11622/smedj.2016095 PMid:27193079 PMCid:PMC5605827

11. Özak, A., Yardımcı, C., Nisbet, Ö.H., Bayrak, İ.K., Nisbet, C. (2010). Evaluation of the effect of platelet-rich plasma on enhancement of bone healing in diaphyseal bone defects by radiography and computed tomography. Ankara Univ Vet Fak Derg. 57, 77-82. https://doi.org/10.1501/Vetfak_0000002314

12. Torres, J., Tresguerres, I., Tamimi, F., Clemente, C., Niembro, E., Blanco, L. (2007). Influence of platelet-rich plasma on bone regeneration: a histomorphometric study in rabbit calvaria. Int J Oral Maxillofac Implants. 22(4): 563-568.

13. Tawfik, A., Kamel, N. (2017). Assessment of autologous platelet gel injection in nonunited long bones. Egypt J Haematol. 42(1): 31-35. https://doi.org/10.4103/1110-1067.206430

14. Santis, D., Nocini, P.F. (2019). Regenerating bone defects using new biomedical engineering approaches (REBORN). Final project report. University of Verona, Verona, Italy.

15. Alonso-Fernández, I., Haugen, H.J., López-Peña, M., González-Cantalapiedra, A., Muñoz, F. (2023). Use of 3D-printed polylactic acid/bioceramic composite scaffolds for bone tissue engineering in preclinical in vivo studies: a systematic review. Acta Biomater. 168, 1-21. https://doi.org/10.1016/j.actbio.2023.07.013 PMid:37454707

16. Li, Y., Chen, S.K., Li, L., Qin, L., Wang, X.L., Lai, Y.X. (2015). Bone defect animal models for testing efficacy of bone substitute biomaterials. J Orthop Translat. 3(3): 95-104. https://doi.org/10.1016/j.jot.2015.05.002 PMid:30035046 PMCid:PMC5982383

17. Zhao, M.D., Huang, J.S., Zhang, X.C., Gui, K.K., Xiong, M., et al. (2016). Construction of radial defect models in rabbits to determine the critical size defects. PLoS One 11(1): e0146301. https://doi.org/10.1371/journal.pone.0146301 PMid:26731011 PMCid:PMC4701453

18. Fisher, J.S., Kazam, J.J., Fufa, D., Bartolotta, R.J. (2019). Radiologic evaluation of fracture healing. Skeletal Radiol. 48(3): 349-361. https://doi.org/10.1007/s00256-018-3051-0 PMid:30238139

19. Salih, S., Blakey, C., Chan, D., McGregor-Riley, J.C., Royston, S.L., Gowlett, S., Moore, D., Dennison, M.G. (2015). The callus fracture sign: a radiological predictor of progression to hypertrophic non-union in diaphyseal tibial fractures. Strategies Trauma Limb Reconstr. 10(3): 149-153. https://doi.org/10.1007/s11751-015-0238-y PMid:26602552 PMCid:PMC4666228

20. Gómez-Barrena, E., Padilla-Eguiluz, N.G., García-Rey, E., Hernández-Esteban, P., Cordero-Ampuero, J., Rubio-Suárez, J.C. (2020). Validation of a long bone fracture non-union healing score after treatment with mesenchymal stromal cells combined to biomaterials. Injury 51(Suppl. 1): S55-S62. https://doi.org/10.1016/j.injury.2020.02.030 PMid:32081389

21. Bujoli, B., Scimeca, J.-C., Verron, E. (2019). Fibrin as a multipurpose physiological platform for bone tissue engineering and targeted delivery of bioactive compounds. Pharmaceutics 11(11): 556. https://doi.org/10.3390/pharmaceutics11110556 PMid:31661853 PMCid:PMC6920828

22. Cavallo, C., Filardo, G., Mariani, E., Kon, E., Marcacci, M., Pereira Ruiz, M.T., Facchini, A., Grigolo, B. (2014). Comparison of platelet-rich plasma formulations for cartilage healing: an in vitro study. J Bone Joint Surg Am. 96(5): 423-429. https://doi.org/10.2106/JBJS.M.00726 PMid:24599205

23. Peng, W., Kim, I., Cho, H., Seo, J., Lee, D., Jang, J., Park, S. (2016). The healing effect of platelet-rich plasma on xenograft in peri-implant bone defects in rabbits. Maxillofac Plast Reconstr Surg. 38, 16. https://doi.org/10.1186/s40902-016-0061-5 PMid:27073798 PMCid:PMC4819464

24. El Backly, R.M., Zaky, S.H., Canciani, B., Saad, M.M., Eweida, A.M., Brun, F., Tromba, G., et al. (2014). Platelet rich plasma enhances osteoconductive properties of a hydroxyapatite-β-tricalcium phosphate scaffold (Skelite™) for late healing of critical size rabbit calvarial defects. J Craniomaxillofac Surg. 42(5): e70-e79. https://doi.org/10.1016/j.jcms.2013.06.012 PMid:23932544

25. Segundo, F.A.S., Costa, E.I.S., de Azevedo, A.S., de Araújo, A.L., Silva, A.C.F., de Lima, G.G., de Sá, M.J.C. (2018). Platelet-rich plasma, hydroxyapatite, and chitosan in the bone and cartilaginous regeneration of femoral trochlea in rabbits: clinical, radiographic, and histomorphometric evaluations. J Healthc Eng. 24, 6917958. https://doi.org/10.1155/2018/6917958 PMid:30034675 PMCid:PMC6035831

26. Shafei-Sarvestani, Z., Oryan, A., Meimandi-Parizi, A., Bigham-Sadegh, A. (2015). Histological, biomechanical and radiological evaluation of bone repair with human platelet-rich plasma in a rabbit model. Zahedan J Res Med Sci. 17(2): e1953.

27. Zamani, M., Kaviani, S., Yousefi, M., Abroun, S., Hojjat-Farsangi, M., Pourabbas, B. (2025). Platelet activation enhances bioactive molecules concentration in platelet-rich plasma. Indian J Hematol Blood Transfus. 4, 1384-1393. https://doi.org/10.1007/s12288-025-02132-6

Please cite this article as: Marinov G.M., Zlateva-Panayotova N.Z., Todorova V.I. Radiological and histological assessment of the regeneration of experimental fractures of critical length, treated with hydroxyapatite alone and in combination with autologous PRP-gel. Mac Vet Rev 2026; 49 (2): 181-194. https://doi.org/10.2478/macvetrev-2026-0021